The Southern Ocean Waves Experiment. Part III: Sea Surface Slope Statistics and Near-Nadir Remote Sensing

E. J. WALSH,*,++ M. L. BANNER,+ C. W. WRIGHT,* D. C. VANDEMARK,# B. CHAPRON,@ J. JENSEN,& AND S. LEE**

*Code 614.6, NASA Goddard Space Flight Center, Wallops Island, Virginia
+School of Mathematics, The University of New South Wales, Sydney, New South Wales, Australia
#Ocean Process Analysis Laboratory, University of New Hampshire, Durham, New Hampshire
@Departement d'Oceanographie Spatiale, Institut Français du Petrole, Plouzané, France
&Research Aircraft Facility, National Center for Atmospheric Research, Broomfield, Colorado
**CSIRO Marine and Atmospheric Research, Aspendale, Victoria, Australia

(Manuscript received 2 February 2007, in final form 30 April 2007)

ABSTRACT

During the Southern Ocean Waves Experiment (SOWEX), registered ocean wave topography and backscattered power data at Ka band (36 GHz) were collected with the NASA Scanning Radar Altimeter (SRA) off the coast of Tasmania under a wide range of wind and sea conditions, from quiescent to gale-force winds with 9-m significant wave height. Collection altitude varied from 35 m to over 1 km, allowing determination of the sea surface mean square slope (mss), the directional wave spectrum, and the detailed variation of backscattered power with incidence angle, which deviated from a simple Gaussian scattering model. The non-Gaussian characteristics of the backscatter increased systematically with the mss, suggesting that a global model to characterize Ka-band radar backscatter from the sea surface within 25° of nadir might be possible.

1. Introduction

For the Southern Ocean Waves Experiment (SOWEX; Banner et al. 1999; Chen et al. 2001; Walsh et al. 2005), conducted in June 1992 out of Hobart, Tasmania, the NASA Scanning Radar Altimeter (SRA; Walsh et al. 1996, 2002; Wright et al. 2001) was shipped to Australia and installed on the CSIRO Fokker F-27 research aircraft, instrumented to make comprehensive measurements of air–sea interaction fluxes. The SRA swept a radar beam of 1° half-power width (two way) across the aircraft ground track over a swath equal to 0.8 of the aircraft height, simultaneously measuring the VV polarization backscattered power at its Ka-band operating frequency (36 GHz, 8.3-mm wavelength) and the range to the sea surface at 64 cross-track positions at measurement angles fixed within ±22° with respect to the normal to the aircraft wings. The transmit angles were tailored to provide the same cross-track displacement between all the points on the sea surface when the aircraft wings were level. The SRA slant ranges were multiplied by the cosine of the off-nadir incidence angles (including the effect of aircraft roll attitude) to determine the vertical distances from the aircraft to the sea surface. Those distances were subtracted from the aircraft height to produce a sea surface elevation map that was displayed on a monitor in the aircraft to enable real-time assessments of data quality and wave properties.

Flights were made on 10, 11, 12, 13, 14, and 16 June 1992. Figure 1 shows the flight pattern on 12 June, which was typical. The aircraft started out at 1-km altitude with (a) an upwind track toward the southwest and (b) a crosswind track toward the southeast to document the directional wave spectrum. It then climbed to 1.2 km and (c) performed a sounding to 23-m altitude. After climbing to 250-m height, (d) data were acquired in a −7° roll attitude (left wing low), turning through

++ On assignment for NASA at the NOAA/Earth System Research Laboratory, Boulder, Colorado.

Corresponding author address: E. J. Walsh, NOAA/Earth System Research Laboratory, PSD3 325 Broadway, Boulder, CO 80305-3337.
E-mail: edward.walsh@nasa.gov

DOI: 10.1175/2007JPO3771.1

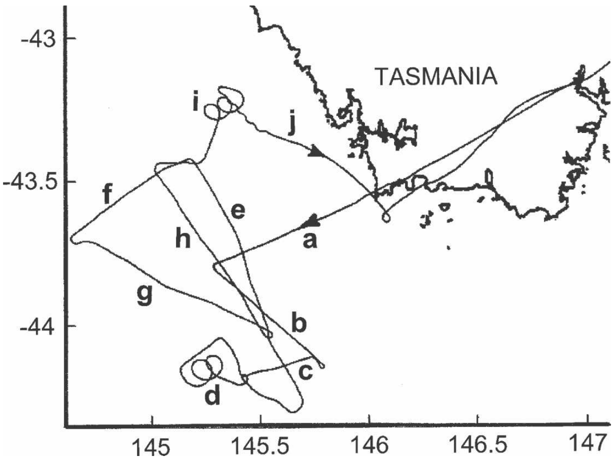

FIG. 1. Aircraft flight pattern on 12 Jun 1992.

two and a quarter revolutions. Then the aircraft descended to 45-m height and flew a triangular pattern to measure stress. The first two legs were oriented (e) crosswind and (f) upwind with (g) the third leg returning to the starting point. After flying (h) a second crosswind segment at 90-m height, the aircraft climbed (i) to 250-m height for a second set of turns. The aircraft then descended to 23-m height before (j) climbing to 1.4 km for the flight back to shore.

Figure 2 is a modification of Fig. 10 in Banner et al. (1999) showing the directional wave spectra measured by the SRA on the six flights with significant wave height, $H_{1/3}$, added above each spectrum. The average U_{10} is indicated below each spectrum with an arrow indicating the dominant downwind direction. On 16 June the wind direction was highly variable (Walsh et al. 2005). The wide range of sea states encountered during this brief experiment proved ideal for studying non-Gaussian scattering from the sea surface at Ka band.

2. Nominal incidence angle dependence of backscattered power

The normalized radar cross section per unit area σ^0 (also called the scattering coefficient) characterizes the ability of a surface to scatter the intercepted energy back toward the radar. Walsh et al. (1998) showed that when the power received by the SRA is multiplied by the square of the range to the surface and the cosine of the off-nadir angle, the result is proportional to σ^0. The SRA was not absolutely calibrated in power and in this analysis we will use variations in the relative backscattered power (the received power modified by the square of the range and the cosine of the incidence angle) interchangeably with σ^0.

The slope-dependent specular point model of radar sea surface scattering is applicable out to incidence angles of about 15° (Barrick 1968). An expression approximated by a geometric optics (GO) form, generalized from Valenzuela's (1978) Eq. (3.8) for the normalized radar cross section in an azimuthal look direction Φ, would be

$$\sigma^0_{GO\Phi} = \rho \sec^4\theta \, \mathrm{mss}^{-1} \exp\{-\tan^2\theta/[2\,\mathrm{mss}(\Phi)]\}, \quad (1)$$

where ρ is an effective reflectivity, θ is the off-nadir incidence angle, and mss(Φ) is the mean square slope of the component of the sea surface slope vector in the azimuthal direction Φ.

For an isotropic, Gaussian surface (Barrick 1974; Valenzuela 1978), mss (Φ) is always equal to mss /2, where mss is the total mean square slope of the sea surface, and (1) can be transformed into

$$\ln(\sigma^0_{\mathrm{rel}}) = -(\mathrm{mss}^{-1} - K)\tan^2\theta, \quad (2)$$

where σ^0_{rel} is the radar cross section normalized by its peak value and $K = \ln(\sec^4\theta)/\tan^2\theta$; K is nearly constant at a value of 2 (Walsh et al. 1998).

The Gaussian assumptions that led to (2) resulted in the peak of the backscattered power occurring at nadir and a linear relationship between the logarithm of the radar cross section and the square of the incident angle tangent. If the isotropic assumption were relaxed, the peak backscattered power would still occur at nadir, but mss in (2) would be replaced by 2 mss(Φ) with the rate of falloff with incidence angle in each azimuthal plane still being linear, but controlled by the mss component in that plane. We will refer to either of those situations as Gaussian backscatter. We will refer to situations where the falloff with incidence angle is not linear and/or the peak of the backscattered power is not at nadir as non-Gaussian backscatter. That is, non-Gaussian backscatter indicates that the backscattered power distribution with incidence angle has excess kurtosis (relative to the value 3 for a Gaussian distribution) and/or its skewness is not zero.

Voronovich and Zavorotny (2001) assumed Gaussian elevation statistics and theoretically computed the incidence angle variation of backscattered power using the small-slope approximation (ssa) and the Elfouhaily et al. (1997) ocean wave spectrum. Their Ku-band (14 GHz, 21-mm wavelength) results for VV polarization at 2° resolution, interpolated to 1° for wind speeds of 5, 10, and 15 m s^{-1}, are indicated by the circles in Fig. 3. Also shown are second-degree curves least squares fitted to the theoretical results for incidence angles between 0° and 29°. The agreement is nearly perfect. The

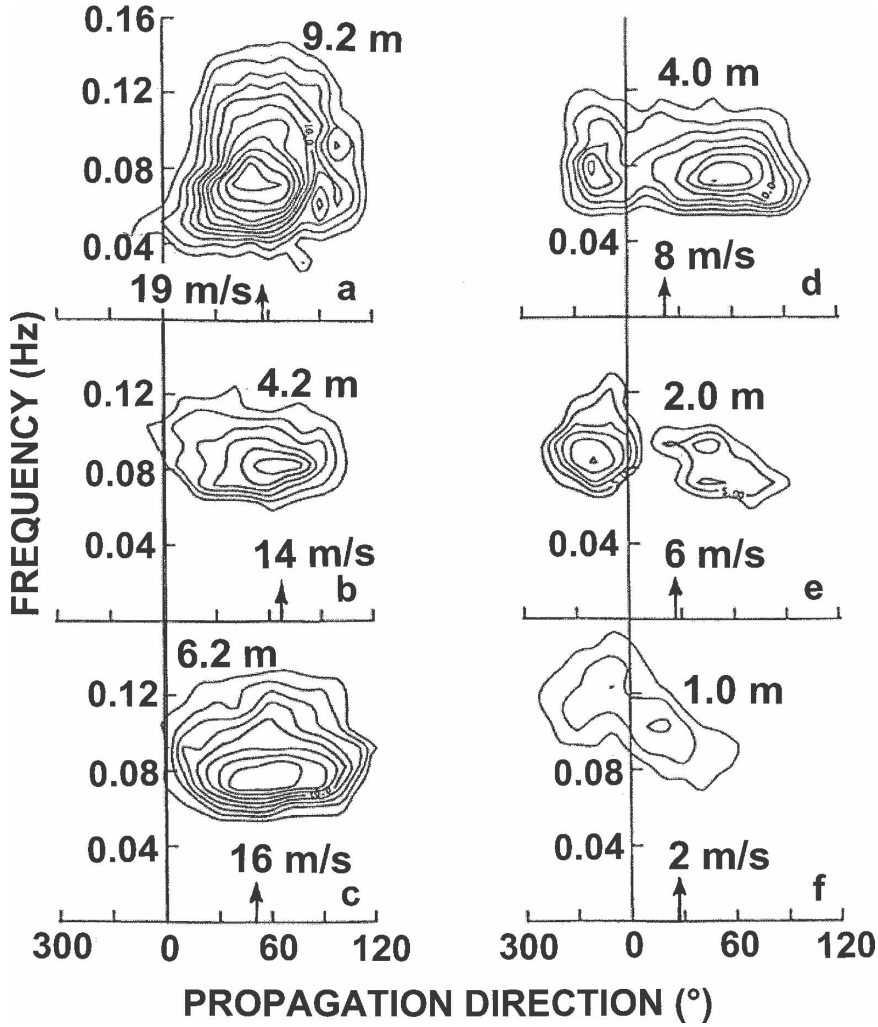

FIG. 2. Directional wave spectra measured by the SRA on (a) 10, (b) 11, (c) 12, (d) 13, (e) 14, and (f) 16 Jun 1992. Significant wave height, $H_{1/3}$, is indicated above each spectrum. The average U_{10} is indicated below each spectrum with an arrow indicating the dominant downwind direction.

Voronovich and Zavorotny (2001) numerical model employing Gaussian sea surface elevation statistics and, therefore, Gaussian slope statistics, resulted in non-Gaussian scattering because it accounted for diffraction.

Alternately, non-Gaussian backscatter could result from the simple geometric optics model that led to (2) in combination with non-Gaussian sea surface slope statistics. Chapron et al. (2000) developed an analytical sea surface slope model using the theory of the surface as a compound process. The compound model concept is often used in a two-scale sense to describe the influence of large-scale inhomogeneities modulating a normally distributed population of smaller scales (Valenzuela 1978).

Chapron et al. (2000) began by assuming a Gaussian slope probability density function (PDF) for an isotropic sea

$$P(S_x, S_y) = \alpha\pi^{-1}\exp(-\alpha S^2), \qquad (3)$$

where α is the inverse of the total slope variance and S is the modulus of the surface slope vector with perpendicular slope components S_x and S_y. If the logarithm of (3) is taken and α_0 is used to explicitly represent the inverse of the total slope variance of a homogeneous sea surface, the result is

$$\ln P(S) = \ln(\alpha_0\pi^{-1}) - \alpha_0 S^2. \qquad (4)$$

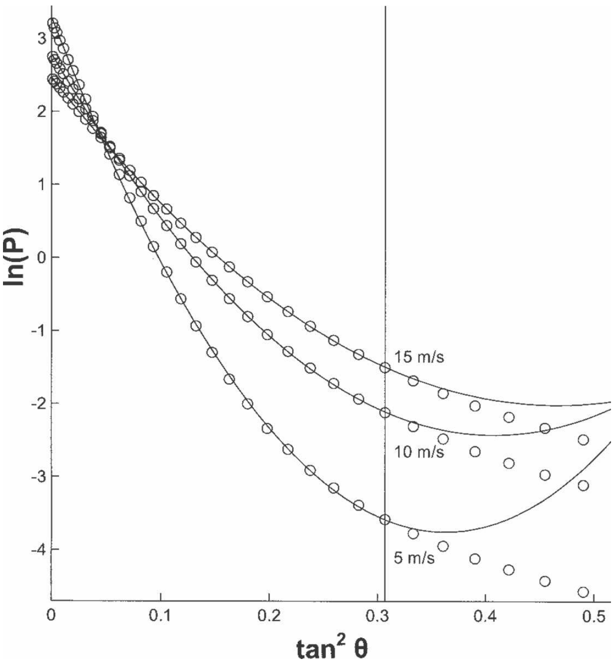

FIG. 3. Circles indicate the theoretical computation for backscattered power variation with incidence angle at Ku band (14 GHz, 21-mm wavelength) for VV polarization and wind speeds of 5, 10, and 15 m s^{-1} (Voronovich and Zavorotny 2001). The second-degree curves were least squares fitted to the theoretical results for incidence angles between 0° and 29° (vertical line).

For the non-Gaussian sea surface, Chapron et al. (2000) considered a collection of randomly distributed patches (on the order of a few meters) where the sea surface slope PDF is locally Gaussian (Gotwols and Thompson 1994), but with the slope variance parameter varying randomly from patch to patch. Modulation transfer function (MTF) studies (Plant 1986) describing short-scale elevation spectral density variability as a function of the underlying long wave are a deterministic parallel to this statistical development.

Chapron et al. (2000) considered α, the inverse of the nonhomogeneous wave slope variance of an individual patch for the nonhomogeneous wave slopes, as perturbations from α_0, the inverse of the overall mean slope variance. They used two different assumptions to characterize the perturbations. In their first development, they assumed that the fluctuations of the inverse slope variance follow a gamma process with mean α_0 and variance $\alpha_0^2\,(1 + \Delta)$. This choice was motivated because it ensured nonnegative values and Γ distributions include a wide range of variations, encompassing exponential distributions as well as almost-Gaussian (not symmetrical about the peak yet still positive) distributions, and using them resulted in analytical forms. The resulting compound slope PDF expansion was

$$\ln P(S) = \ln(\alpha_0\pi^{-1}) - \alpha_0(1 + \Delta)S^2 + 0.5\alpha_0^2\Delta(1 + \Delta)S^4 + \cdots. \tag{5}$$

Their alternate development represented α as

$$\alpha = \alpha_0(1 + \delta), \tag{6}$$

where δ is a zero mean random fluctuation modulating the inverse of the overall mean slope variance.

If the variance of the random fluctuation δ is Δ, they determined that the logarithm of the compound PDF restricted to slope terms of the fourth power would be

$$\ln P(S) = \ln(\alpha_0\pi^{-1}) - \alpha_0(1 + \Delta)S^2 + 0.5\alpha_0^2\Delta(1 - \Delta)S^4 + \cdots. \tag{7}$$

[The 0.5 factor in (7) was inadvertently omitted from the last term of the comparable Eq. (20) of Chapron et al. (2000).] The expressions (5) and (7), developed from different assumptions, are nearly identical. The difference is that the Δ^2 term is positive in (5) and negative in (7).

At this point we expand upon the Chapron et al. development and examine the characteristics of (5) and (7) in detail because they potentially provide a means to estimate Δ from the observations of the falloff of backscattered power with incidence angle.

Consider the general expression

$$\ln P(S) = -AS^2 + BS^4, \tag{8}$$

which is similar to (5) and (7) except that the constant term has been deleted, essentially normalizing (3) by its peak value. With the change of variables

$$Z = AS^2, \tag{9}$$

(8) becomes

$$\ln P(S) = -Z + RZ^2, \tag{10}$$

where $R = A^{-2}B$. Figure 4 is a plot of (10) for values of R from 0 to 0.1; R is a measure of the nonlinearity of the curve. When $R = 0$, the curve is a straight line. When R is nonzero, the slope of the curve becomes zero at

$$Z = (2R)^{-1}, \tag{11}$$

a factor $(4R)^{-1}$ below the peak. With the variable Z normalizing every linear decay rate to unity, R is a measure of the fraction of the peak value at which the curve becomes noticeably nonlinear.

The expression for R corresponding to (5) is

$$R_5 = 0.5\Delta(1 + \Delta)^{-1}, \tag{12}$$

and corresponding to (7) it is

$$R_7 = 0.5\Delta(1 - \Delta)(1 + \Delta)^{-2}. \tag{13}$$

Figure 5 shows plots of R_5 (+) and R_7 (o).

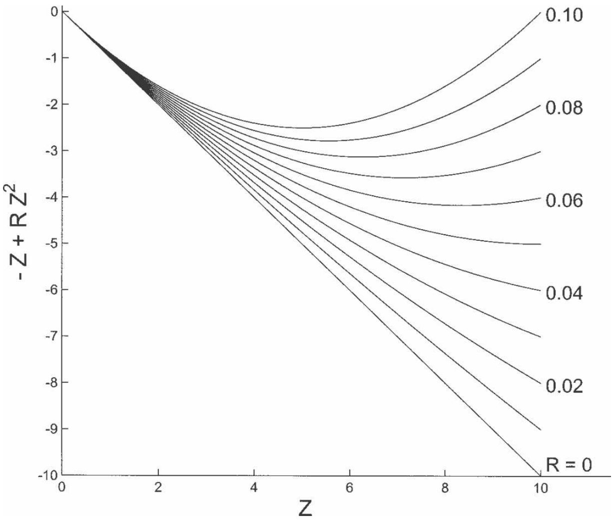

FIG. 4. Plot of Eq. (10) for values of R from 0 to 0.1.

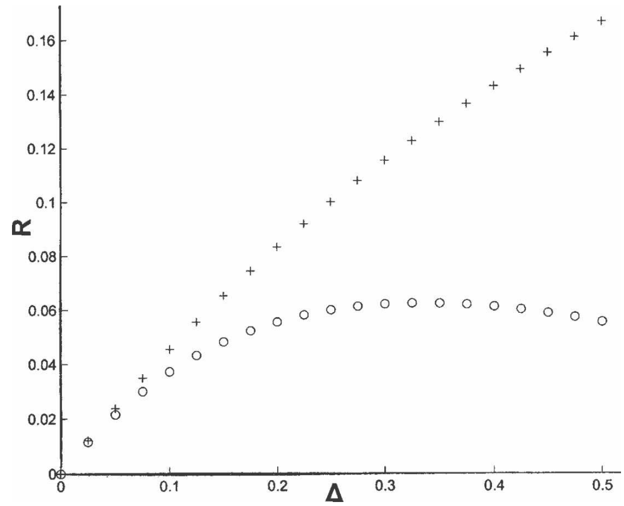

FIG. 5. Plots of Eqs. (12) (+) and (13) (o).

If (12) is solved for Δ, the result is

$$\Delta_5 = 2R(1 - 2R)^{-1}. \tag{14}$$

Similarly, (13) produces

$$\Delta_7 = [1 - 4R - (1 - 16R)^{0.5}](2 + 4R)^{-1}. \tag{15}$$

When R is very small, (14) and (15) both reduce to $2R$. But (15) provides a complex result when $R > 0.0625$, the maximum value of R_7 shown in Fig. 5. This is an unreasonably low limitation on R since some of the SRA measurements of R exceed 0.1. The expression (14) for Δ_5 is well behaved for $R < 0.5$.

The difficulty with (15) may have resulted in the way the perturbation was defined. In (6), α is a zero mean process in δ but not in S^2. The mean value α will be α_0, but the mean value of S^2 will not be $(\alpha_0)^{-1}$, which the direct comparisons of terms from (5) and (7) implicitly assume. As the value of δ increases, the mean value of α remains the same, but the mean value of S^2 grows as the standard deviation of δ increases. For a standard deviation of 0.2, the increase is a little under 5%. A standard deviation of 0.333 increases S^2 by over 26%. The Γ distribution is asymmetrical with zero probability of values less than zero. It cannot produce negative values for large standard deviations, which can occur with a symmetrical distribution.

Although (14) appears to be the more reasonable expression, it should be emphasized that in neither development was the value of Δ related to α_0, which indicated the magnitude of the mss itself; R and Δ were simply measures of the nonlinearity that could be associated with any value of mss. In analyzing the SRA data, we will compute the A and B in (8) using second-order least squares fits to the backscattered power incidence angle variation and assume from (14) that

$$\Delta = 2R(1 - 2R)^{-1}, \tag{16}$$

which allows the computation of the mss (i.e., α_0^{-1}) from (5) as

$$\text{mss} = [1 + 2R(1 - 2R)^{-1}]A^{-1}. \tag{17}$$

3. Azimuthal variation of wave topography and backscattered power

On each flight, data were acquired at 250-m altitude while the aircraft was nominally in a −7° roll attitude (left wing low), interrogating off-nadir incidence angles from −15° through nadir to +29° (Fig. 6). The aircraft turned azimuthally through 810° in this attitude, mapping the azimuthal dependence of the backscattered power falloff with incidence angle. Two sets of turning data were acquired on most days, before and after the aircraft measured wind stress at low altitude (12 to 65 m, depending on conditions). But, due to various problems there was only one set of turning data that did not need special editing on each day except on 12 June, when both sets were good. Wave topography and backscattered power for mss were also acquired during level flight segments whenever the aircraft altitude was above the SRA minimum range of about 30 m.

Figure 7 shows the aircraft heading and the wind direction at the 250-m aircraft altitude for a portion of the first set of turning data on 12 June. The SRA directional wave spectrum was unimodal (Fig. 2) with the spectral peak, indicating that the dominant waves prop-

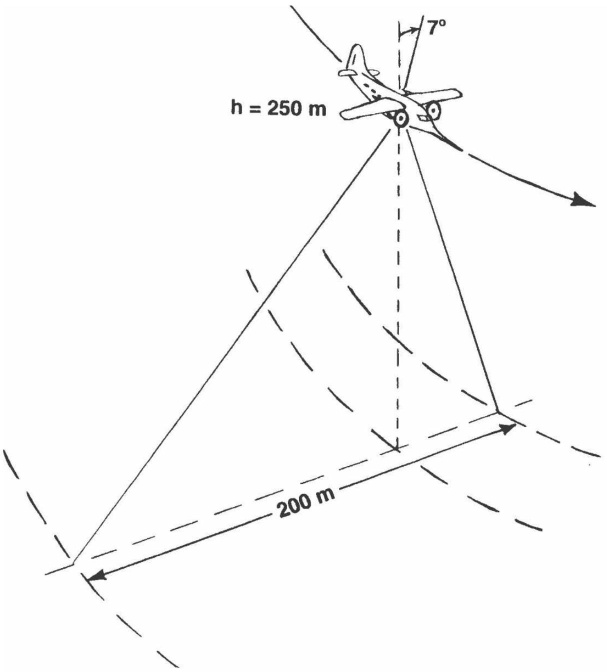

FIG. 6. Measurement geometry for data acquired at 250-m altitude while the aircraft was in a −7° roll attitude.

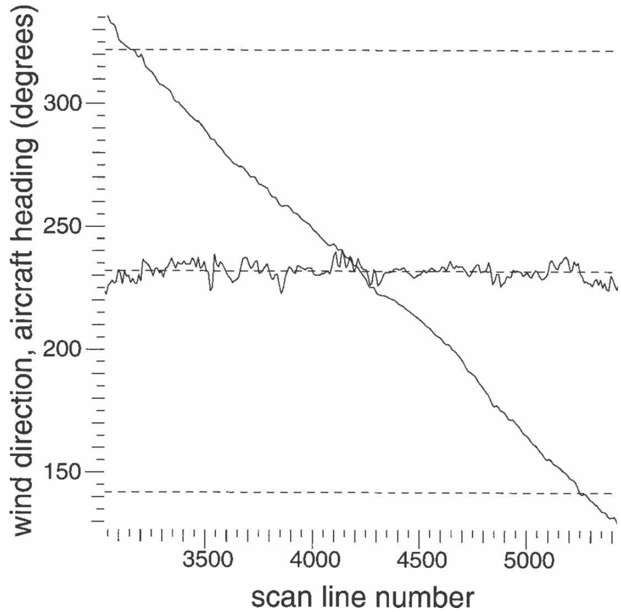

FIG. 7. Aircraft heading, varying almost linearly with scan line number from 337° to 127°, and the wind direction (from approximately 232°) at the 250-m aircraft altitude for a portion of the first set of turning data on 12 Jun 1992 in the vicinity of 44.2°S, 145.3°E (Fig. 1).

agated toward 55° with a phase speed of 20.6 m s^{-1} (275-m wavelength). This was nearly identical to the mean wind vector at the aircraft altitude (21.7 m s^{-1} toward 52°). Waves evolve as they propagate, but to first order the wind vector at the aircraft altitude nearly matching the dominant wave propagation vector can be thought of as producing an equivalent dataset as an aircraft flying in circles at its 75 m s^{-1} airspeed on a windless day over a wave field fixed in space.

This alternate view produces a relatively undistorted image of the topography and is much simpler to implement than vector adding the phase speed of the waves to the aircraft ground speed, which changed continuously between 96 m s^{-1} when the aircraft was heading downwind and 54 m s^{-1} when it was heading into the wind. Figure 8 shows this simple presentation of the SRA wave topography and backscattered power for the data span indicated in Fig. 7. With the SRA 9.4-Hz scan rate, the aircraft advanced 8 m per scan line. The along-track data point spacing in Fig. 8 is 2.5 times the cross-track spacing, providing images of the waves that are in correct proportion locally and automatically rectifying the circular track over the ocean.

In the contiguous data span shown in Fig. 8, the aircraft took 4.3 min to turn through 210° and covered an effective along-track distance of about 19 km. It is broken into five segments with time (and distance around the circle) advancing up the page and from left to right. The aircraft heading changed continuously, but at the start of the first segment it was nearly crosswind (Fig. 7) with the aircraft flying parallel to the dominant wave crests and the SRA scan plane looking downwind on the right side of the swath. In the middle segment the aircraft was flying nearly upwind, perpendicular to the crests of the dominant waves, and the SRA scan plane was looking in the crosswind direction. In the fifth segment the aircraft was again flying nearly parallel to the wave crests, but with the SRA scan plane looking upwind on the right side of the swath.

The left image of each pair is grayscale-coded wave topography (troughs dark, crests light). The significant wave height was 6.2 m, and the nadir channel of the 64 cross-track positions has been colored white. The right image of each pair is the backscattered power with the incidence angle (cross-track) dependence removed by normalizing each power value by the average value of power at that off-nadir incidence angle for that segment.

The aircraft heading in degrees at the beginning and end of each segment is indicated below and above each pair of images, respectively. Each of the five segments contains the same time span (481 scan lines of data), but the change in aircraft heading over each segment varies between 50° and 35° instead of the 42° average value due to variations in aircraft roll attitude.

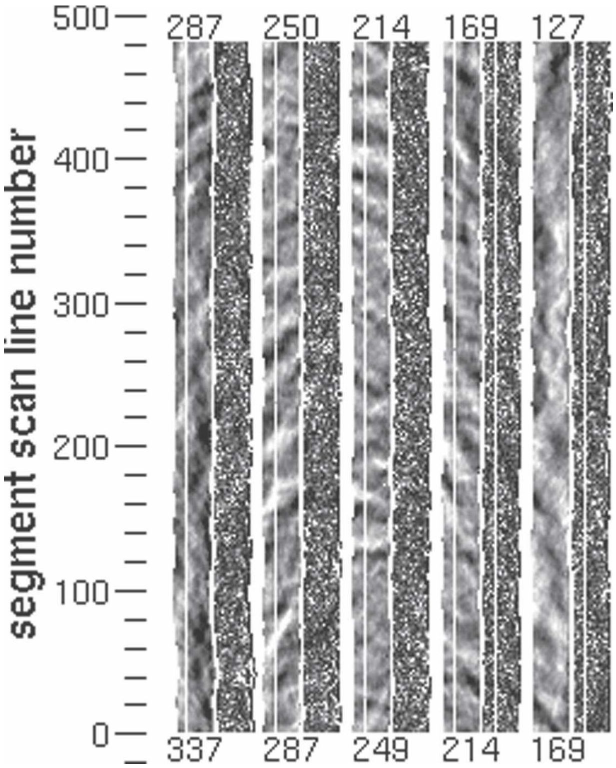

FIG. 8. SRA (left) wave topography and (right) backscattered power for the data span indicated in Fig. 7, broken into five segments, with the starting and ending aircraft headings indicated below and above each segment. The average cross-track variation of the backscattered power in each segment has been removed.

4. Eliminating long-scale surface tilt contamination

It was desired to examine the variation of the scattering characteristics relative to the wind direction using 15° azimuthal bins. But Fig. 8 indicates that the 88 scan lines (700-m along-track distance) typically covered during a 15° heading change were not sufficient to ensure that the along-track and cross-track surface slopes associated with the longer waves would be statistically represented at every cross-track (off-nadir incidence angle) position.

Thompson and Gotwols (1994) and Gotwols and Thompson (1994) investigated the effect of sea surface slope modulation of local incidence angle using data from a Ka-band scatterometer boresighted at 17° off-nadir, an X-band (10 GHz, 30-mm wavelength) scatterometer boresighted at 20° off-nadir, and Ku-band scatterometers boresighted at 20° and 45° off-nadir. At the 17° and 20° incidence angles they found that the modulation of the backscattered power was so dominated by the large-scale wave slopes that they could reproduce its general characteristics without having to incorporate in their scattering model the modulation of the short-wave spectral density over the long-wave phase. At 45° off-nadir, the long-wave slopes were less dominant and their model could not reproduce the observations unless they incorporated hydrodynamic modulation of the short-wave spectral density as a function of its position along the long-wave surface.

Since the area bounded by each 15° azimuthal interval used in the present study contained so few dominant wavelengths, not considering their slopes would badly corrupt any attempt to determine the general incidence angle and azimuthal dependence of the backscattered power. Because the scatterometers used by Thompson and Gotwols (1994) did not measure range, they could not document the topography of individual waves as the SRA could, so their modeling analysis was indirect. In the present study we directly mitigated the long-wave corrupting effect by using the along- and cross-track slopes computed from the SRA wave topography measurements to determine local incidence angles for binning the backscattered power data.

The cross-track surface slope at each cross-track position n on a given SRA scan line was taken as the slope of a straight line least squares fitted through nine adjacent elevations ($n \pm 4$). This reduced the useable swath from cross-track positions 1–64 to 5–60. The along-track slope was determined at each position, n, on a given SRA scan line by subtracting the average of five elevations ($n \pm 2$) from the previous scan line from the same five-elevation average on the following scan line and divided by the 16-m distance between those lines. Several algorithms were tried, but these were subjectively judged to provide the best results.

The cross-track slope determination was the more critical of the two with its greater impact on the local incidence angle at the edges of the swath because it was directly added to the antenna off-nadir boresight angle. Nine points were used to minimize noise generated by errors in the elevation measurements while still providing a reasonable estimate of the midpoint surface slope even if the surface curved within the 25-m span. At the SRA 9.4-Hz scan rate and 50% duty cycle, the duration of each cross-track scan was about 0.05 s. The sea surface could be assumed frozen during the 7-ms time interval needed to acquire each set of nine points used in the cross-track slope determinations.

The sea surface could not be assumed frozen during the 0.2-s interval between the previous and following scan lines for the along-track slope determination, but the discussion in section 3 justified the simple computation using the aircraft airspeed on 12 June. On 10 June, the 300-m wavelength dominant waves propagated at 21.6 m s^{-1} toward 50°, also nearly matching the wind speed at the aircraft 250-m altitude, which was

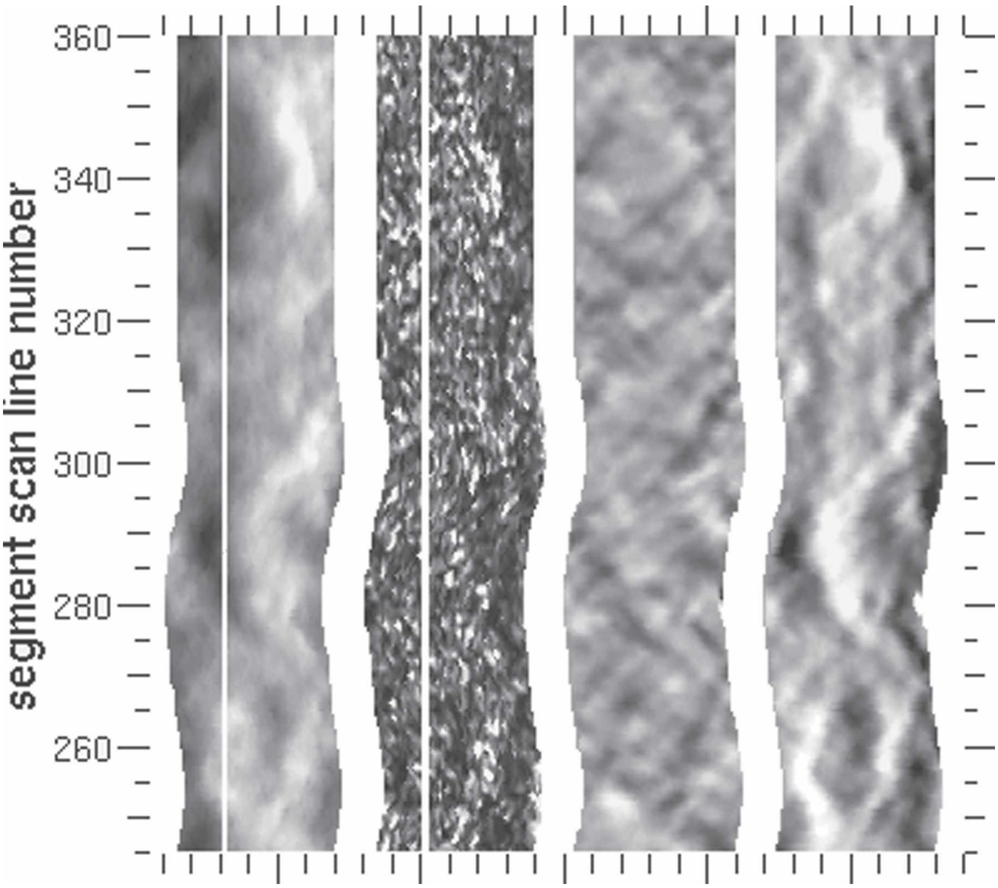

FIG. 9. (left), (second) An enlargement of a portion of the fifth segment of Fig. 8. (third) The along-track and (fourth) cross-track sea surface slopes.

24.5 m s^{-1} toward 60°. On 11 June, the 240-m wavelength dominant waves propagated at 19.3 m s^{-1} toward 65°, fairly well matching the wind speed of 15.3 m s^{-1} toward 68° at the 250-m aircraft altitude.

The conditions were not as fortuitous on 13 June when the wind speed at the 250-m aircraft altitude was 9.4 m s^{-1} toward 24°. There was a bimodal wave system with the 300-m wavelength propagating at 21.6 m s^{-1} toward 340° and the 240-m wavelength propagating at 19.3 m s^{-1} toward 55°. If wind and wave directions had been aligned, a 12 m s^{-1} difference between wind speed and phase speed would cause minimal error in the along-track slope computation when the aircraft was flying parallel to a wave crest. It would cause 2.4-m (15%) changes in the nominal 16-m baseline used in the simple computation when the aircraft was heading upwind or downwind. But the situation on 13 June was more complex because the wave propagation directions deviated 30° and 45° in opposite directions from the downwind direction. Under those circumstances it would be difficult to even assign a speed and direction to a particular point on a wave. The simple correction was considered better than none.

On 16 June, the wind speed was negligible and the 16 m s^{-1} phase speed of the waves would cause 20% errors in the nominal baseline for the along-track slope determination when the aircraft was heading either upwave or downwave. But the simple along-track slope corrections would be in the proper direction and, with the wave height much lower than on 10 or 12 June, the absolute size of the errors would be small.

There is no guarantee that surface slopes not resolved by these computations were associated with ocean waves short enough to be assumed statistically uniform at every cross-track position over any 700-m along-track distance. But, at least the major corrupting influence of the dominant wave slopes was eliminated.

Starting from the left in Fig. 9, the first two images are an enlargement of a portion of the fifth segment of Fig. 8 when the right side of the SRA scan plane was directed approximately upwind. The third and fourth images are the along-track and cross-track sea surface

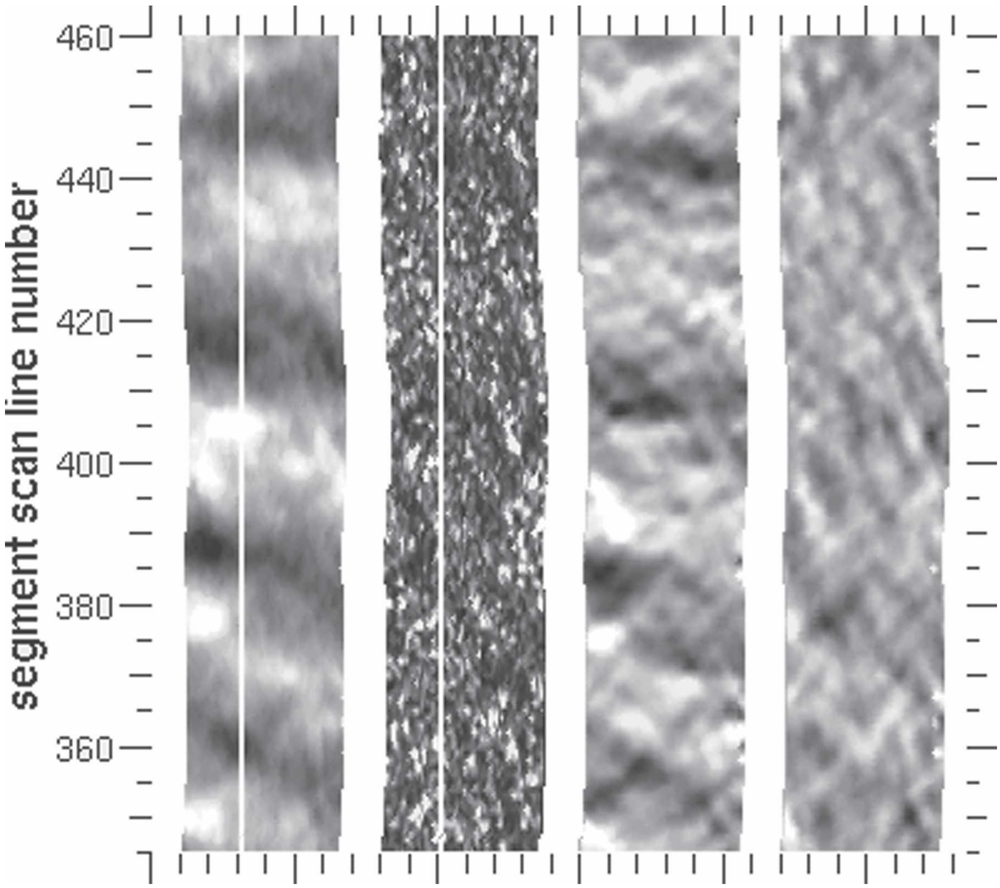

FIG. 10. As in Fig. 9, but for a portion of the third segment of Fig. 8.

slopes (white: maximum positive slope, black: maximum negative slope) determined by the SRA in the manner just described.

Figure 10 shows an enlargement of a portion of the third segment of Fig. 8 with the associated along-track and cross-track slopes. Although the SRA scan plane in Fig. 10 was an average of about 15° off the mean crosswind direction, this interval was selected because the dominant wave slopes were nearly in the along-track direction. Figures 9 and 10 only display cross-track positions 5 through 60 because of the limitations imposed by the cross-track surface slope computation. In both Figs. 9 and 10, the slope determinations do not appear to be noisy, and the largest slopes are in the dominant wave propagation direction.

Figure 11 plots the surface elevation and along-track and cross-track surface slopes for 88 scan lines from cross-track position 11 (of 64 starting from the left) of Fig. 10, which represents the average time interval for a 15° change in aircraft heading during the turning segments. The largest along-track slopes have magnitudes of about 10°. The largest cross-track slopes are in the 5°–7° range.

The cross-track slope determinations are totally independent from scan line to scan line because they only involve the surface elevations on their own scan line. Yet they map out a smooth progression in Fig. 11 with little jitter. Adjacent along-track slope determinations are independent, but they also display little jitter in Fig. 11.

5. Skewness in backscattered power distribution

The seminal work of Cox and Munk (1954) measured the statistics of the sun's glitter to determine the sea surface slope distribution. There have since been many measurements using a variety of techniques (Hughes et al. 1977; Tang and Shemdin 1983; Haimbach and Wu 1985; Hwang and Shemdin 1988; Wu 1991; Bock and Hara 1995; Shaw and Churnside 1997) confirming and extending the Cox and Munk results that, when wind and waves are aligned, the slope PDF is nearly Gaussian in the crosswind direction and significantly departs from Gaussian in the upwind–downwind direction.

Cox and Munk chose to demonstrate the characteristics of the slope distribution by showing two curves

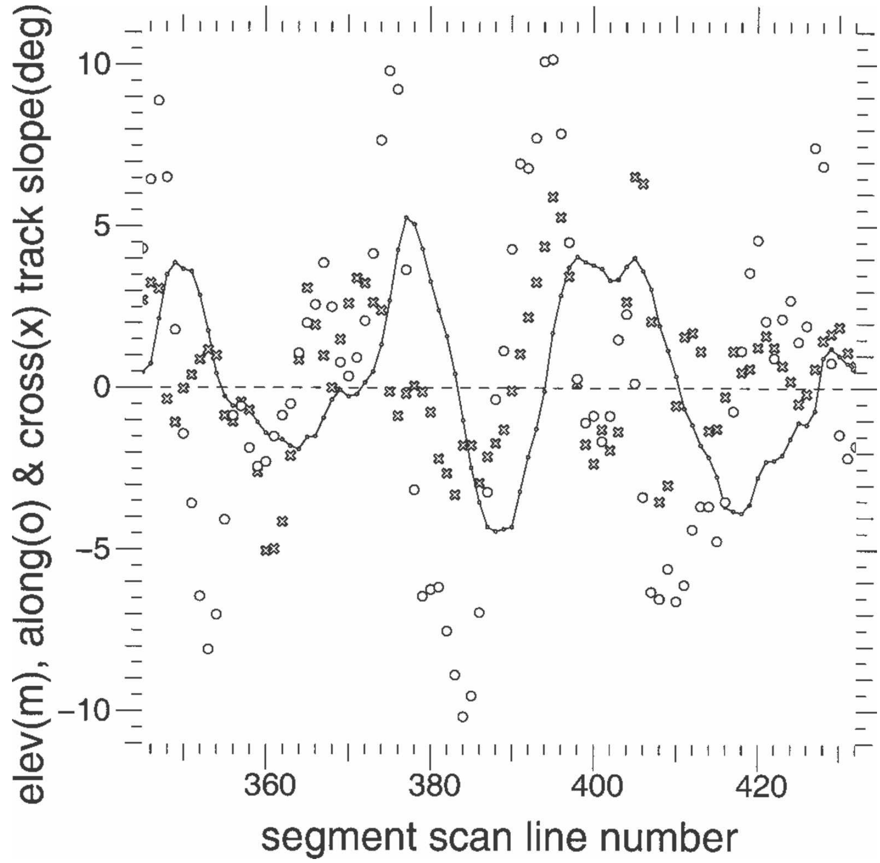

FIG. 11. Surface elevation (dots connected by straight lines) and along-track (o) and cross-track (×) surface slopes for 88 scan lines from cross-track position 11 (of 64 starting from the left) of Fig. 10.

corresponding to a 12.5-m height wind speed of 10 m s^{-1}. One curve showed the slope distribution in the crosswind plane to be perfectly symmetrical about nadir with a standard deviation of 8°. Its small and large slopes were more probable than for a corresponding Gaussian distribution of the same mss, indicating kurtosis, but not skewness. The Cox and Munk curve for the upwind–downwind plane is reproduced in the top panel of Fig. 12. It had a larger standard deviation (10°) than the crosswind direction and the peak of the distribution was shifted off-nadir 2.9°. Small slopes were also more probable than for a Gaussian distribution of the same mss (dashed curve), indicating kurtosis in addition to the skewness.

The Cox and Munk curve indicates that slopes in the upwind direction (to the right) have a higher probability than slopes in the downwind direction for incidence angles greater than 25°. This is reassuring since scatterometers operating in that incidence angle region see higher backscatter in the upwind direction than in the downwind direction. However, care must be taken interpreting the Cox and Munk curve in that region because they did not have observations at angles greater than 15°. The truncated Gram–Charlier expansion that Cox and Munk, and most other investigators, have used in interpreting observations is not a true PDF because false negative probabilities can appear, raising questions about its ability to extrapolate (Tatarskii 2003). It is even apparent that the Cox and Munk curve is about to go negative at its left limit in Fig. 12.

Of greater significance to the present study is that the near-nadir distribution has nearly perfect symmetry within about 15° of its peak, where the fitted curve should have well represented the Cox and Munk observations. The middle panel of Fig. 12 is from Walsh et al. (1998) and shows alternative plots of the Cox and Munk fitted curve. The circles are values scaled off the Cox and Munk graph and plotted using the original off-nadir values. The dashed curve corresponds to the expected power variation for a surface whose mss = 0.045 if it were tilted up in the downwind direction by 2.9°, or if it were horizontal but the off-nadir angles of

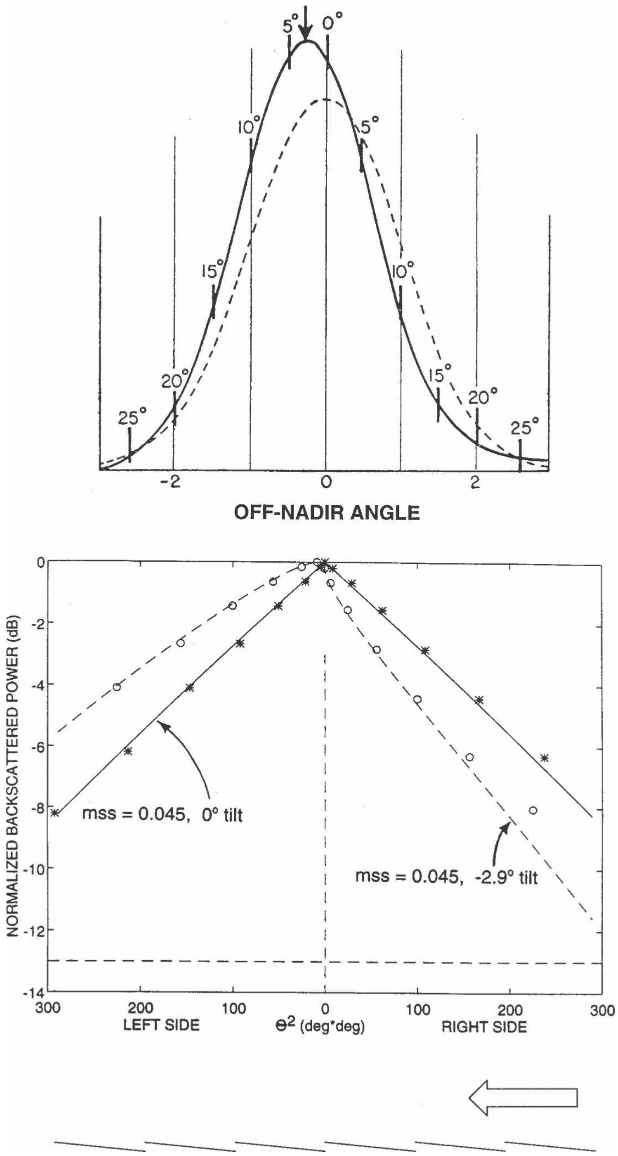

FIG. 12. (top) A reproduction of the Cox and Munk (1954) plot of the sea surface slope distribution in the upwind–downwind plane for a 10 m s^{-1} wind speed. The abscissa scale is in terms of the observed standard deviation of the surface tilts (10° in this instance). (middle) The Cox and Munk values (circles) and an alternative plot (asterisks) shifting the Cox and Munk incidence angles by 2.9°. (bottom) The arrow indicates the downwind direction and shows a simple ad hoc surface model that would produce the near-nadir observations.

the antenna boresight were in error by 2.9°. The asterisks are the same data values as the circles but with the associated incidence angles shifted by 2.9°. The asterisks are very close to the solid curve corresponding to a horizontal surface within about 12° of the peak.

The dashed curve in the middle panel of Fig. 12 suggests that ignoring an off-nadir bias in the peak of the backscattered power distribution will result in a poorer understanding of the nature of the scattering. Since (4) indicates that the slope of the fall-off of backscattered power with incidence angle is inversely proportional to the mss, the small slope of a straight line least squares fitted to the circles to the left of nadir would indicate a large mss on that side of the swath, while the large slope of a straight line least squares fitted to the circles to the right of nadir would indicate a small mss on that side of the swath. That would erroneously suggest a discontinuity in small-scale roughness at nadir.

Because the dashed curve is about as far above the solid (symmetrical) curve on the left side as it is below it on the right side, the effect of ignoring skewness in the distribution could be mitigated to first order and a reasonable value of mss obtained by averaging the data from the two sides of the swath. That was not the approach taken in the present study. A parabola was fitted to the SRA data in the vicinity of nadir (Walsh et al. 1998) within each 15° azimuthal bin relative to the wind direction to determine any deviation from nadir in the peak of the backscattered power distribution.

The bottom of Fig. 12 shows a physically unrealistic, ad hoc surface model that would produce the near-nadir Cox and Munk observations shown in the top panel. Suppose that the overall surface were horizontal and of uniform mss but segmented into a series of strips extending in the crosswind direction with each strip tilting up 2.9° in the downwind direction. The vertical scale in the figure has been magnified by a factor of 2 for clarity.

What would be predicted by the ad hoc model as the SRA scan plane rotated azimuthally? The peak of the backscattered power distribution in any azimuthal plane of incidence would be expected to occur when the off-nadir incidence angle was closest to the effective normal to the surface. If $\mathbf{u}_x$, $\mathbf{u}_y$, and $\mathbf{u}_z$ are the unit vectors in the x, y, and z directions, the unit vector normal to a surface effectively tilted up at an angle θ_p in the y direction would be

$$\sin\theta_p \mathbf{u}_y + \cos\theta_p \mathbf{u}_z. \tag{18}$$

The unit vector at an off-nadir angle θ in a vertical plane whose azimuth is at an angle φ with respect to the vertical plane through the y axis would be

$$\sin\varphi \sin\theta \mathbf{u}_x + \cos\varphi \sin\theta \mathbf{u}_y + \cos\theta \mathbf{u}_z. \tag{19}$$

The angle between the two vectors is minimized when their inner product is minimized:

$$d/d\theta(\cos\varphi \sin\theta \sin\theta_p + \cos\theta \cos\theta_p) = 0, \tag{20}$$

which, for small values of θ_p, reduces to

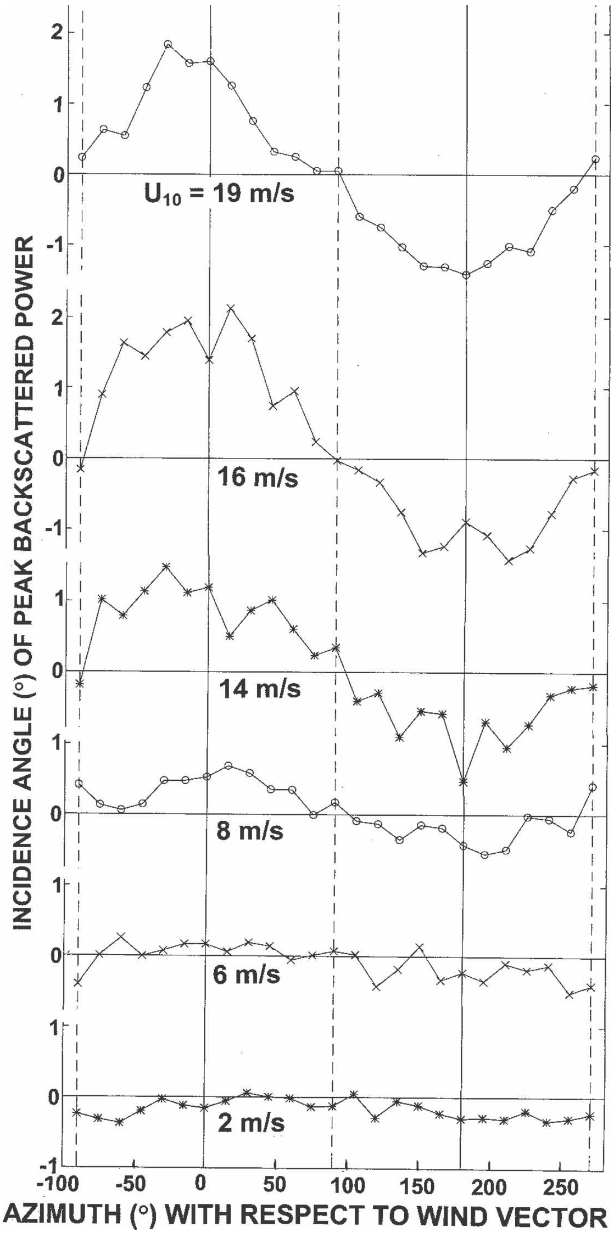

FIG. 13. Azimuthal variation of the incidence angle of the peak of the backscattered power for a set of turns from each of the six flights.

$$\theta = \theta_p \cos\varphi. \tag{21}$$

The off-nadir angle of the peak of the backscattered power distribution would vary sinusoidally with the azimuth of the angle of the incidence plane with respect to the wind direction.

Figure 13 is a plot of the azimuthal variation of the incidence angle of the peak of the backscattered power for a set of turns from each of the six flights. For the days when the wind speed was 2 and 6 m s^{-1}, it is difficult to discern any azimuthal signature. An azimuthal variation is apparent at 8 m s^{-1} with an amplitude of about 0.5°, increasing to about 1.3° at 14 m s^{-1} and over 1.5° at 16 and 19 m s^{-1}.

The characteristics of near-nadir backscatter could also be thought of in terms of two other very simple two-scale models that do not have the discontinuities of the saw-toothed sea surface shown in the bottom panel of Fig. 12. One assumes that the small-scale roughness is uniform spatially but the large-scale waves have bound second harmonics that increase the wave steepness on the leading edge and decrease it on the trailing edge, skewing the large-scale wave slope distribution. An alternate view would be to assume a Gaussian distribution of the large-scale wave surface slopes with a spatial variation of small-scale roughness that was minimum on the rear faces of the waves, larger at the crests, and maximum on the forward faces. For such a surface, the highest specular backscatter would occur when looking off-nadir in the downwind direction, normal to the smoothest part of the large-scale waves even though the peak of their slope distribution was at nadir.

Tatarskii (2003) developed a method to decompose an arbitrary PDF as the sum of displaced Gaussian functions and demonstrated its application using the Cox and Munk (1954) slope dataset and the complex Huang and Long (1980) surface elevation dataset. Plant (2003) also reanalyzed the Cox and Munk (1954) dataset using the sum of two displaced Gaussian PDFs and adding a physical interpretation. One PDF represented the wind-generated free waves, while the other represented the bound waves that travel at nearly the phase speed of the longer waves that generate them. The PDF of the wind-generated waves was shifted toward the upwind side of the crests, which would cause the apparent shift of the peak of the backscattered power seen in the SRA data. The broader, lower PDF of the bound waves in Plant's analysis is shifted even further, but in the opposite direction, toward the steep forward face of the longer waves, producing the higher slope probabilities observed at larger angles in the upwind direction.

Surface slopes on distances longer than about 25 m in the cross-track direction and 16 m in the along-track direction were effectively eliminated in the SRA data processing. This might explain why the maximum displacements of the scattering peak from nadir observed by the SRA are smaller than the Cox and Munk 2.9° value.

6. Kurtosis in backscattered power distribution

Figure 14 shows the mean variation of backscattered power versus local incidence angle for the SRA scan

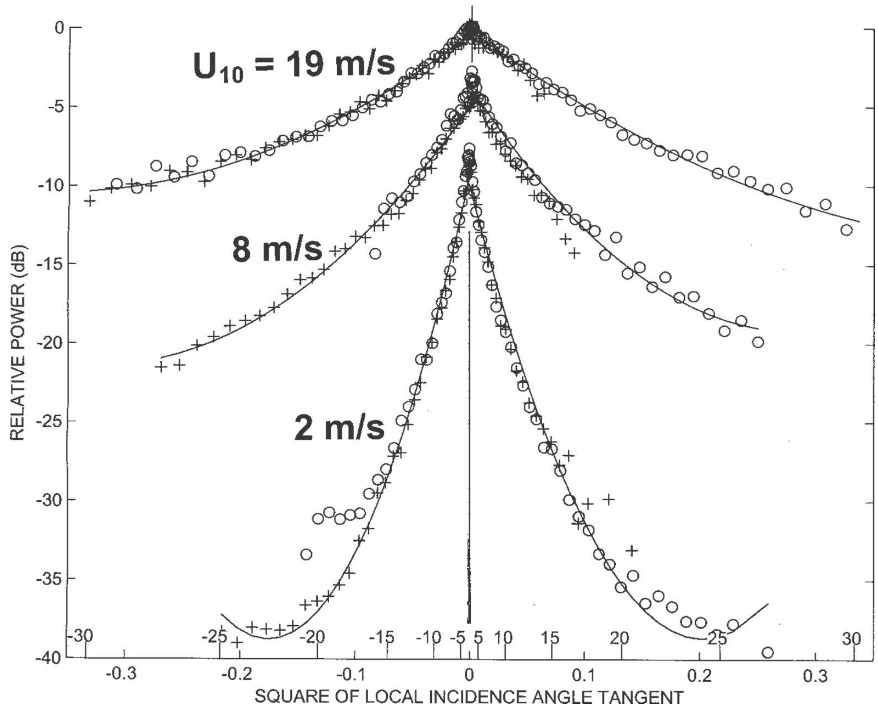

FIG. 14. Backscattered power variation for the SRA scan plane within ±7.5° of the upwind–downwind direction with positive angles indicating the downwind direction. Circles indicate data for which the right side of the SRA scan plane was oriented downwind, and + symbols indicate the data for which the right side of the scan plane was oriented upwind. The data for 8 m s^{-1} were shifted down by 10 dB and the data for 2 m s^{-1} were shifted down by 15 dB. The second-order curves on the right side were least squares fitted to the circles, and the curves on the left side were least squares fitted to the + signs.

plane within ±7.5° of the upwind–downwind direction, with positive numbers indicating the downwind direction. The nadir power increased as the wind speed decreased, but for clarity the data for 8 m s^{-1} were shifted down by 10 dB and the data for 2 m s^{-1} were shifted down by 15 dB so that they would not overlap.

The SRA data were first placed in local incidence angle bins determined from the antenna boresight angle and the along- and cross-track surface slopes. Then a parabola fitted to the SRA data in the vicinity of nadir (Walsh et al. 1998) determined any deviation from nadir of the peak of the backscattered power distribution, and that off-nadir angle was subtracted from all the angle values before plotting in Fig. 14. A second-order curve was then fitted to the backscattered power values on the right side of the distribution peak. Curves were fitted to the data to the right side of the peak because in a −7° roll attitude the incidence angle extended out to 29° off-nadir to the right but only to 14° off-nadir to the left. The swath width limitation imposed by the cross-track slope determination reduced those values to about 26° on the right side and 11° on the left.

The circles in Fig. 14 indicate the data points for which the right side of the SRA scan plane was oriented in the downwind direction, and the plus symbols (+) indicate the data for which the right side of the scan plane was oriented toward the upwind direction. The second-order curves on the right side of Fig. 14 were least squares fitted to the circles, and the curves on the left side were least squares fitted to the plus signs.

There were generally brief straight-and-level segments flown just before and after the turning segments, which extended the range of angles past the nominal 11° limit on the left side of the swath in the crosswind and up/downwind scan planes, as did variations in aircraft roll attitude. But to be consistent with the limits in the intervening azimuthal directions, only curve fits to the data on the right side of the swath were used throughout.

The circles in Fig. 15 indicate the variation of R (10) versus mss (17) for the 8-mm wavelength SRA data from the six SOWEX flights. The three plus symbols indicate the R values corresponding to the 21-mm wavelength (Fig. 3) theoretical computation by Voronovich and Zavorotny (2001). The nonlinearity

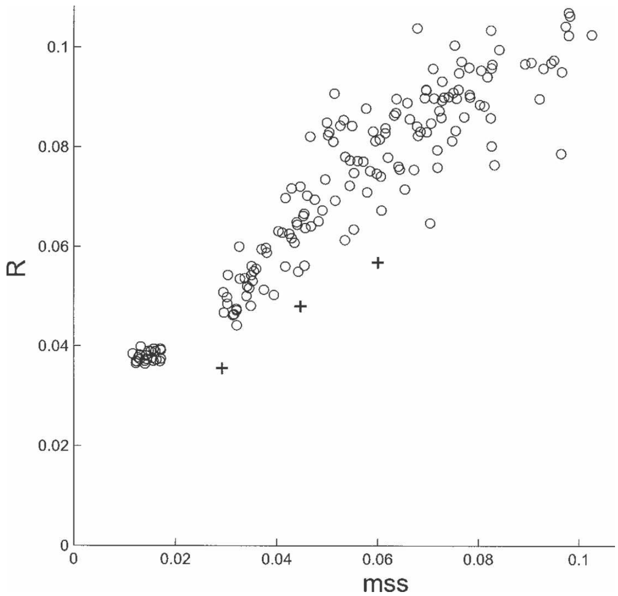

FIG. 15. Variation of R vs mss for the 8-mm SRA data (circles) from the six SOWEX flights and the theoretical computation by Voronovich and Zavorotny (2001) at 21-mm wavelength (+).

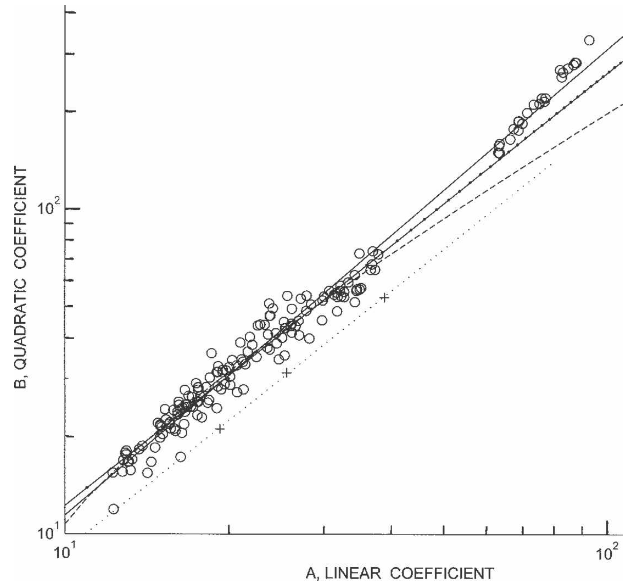

FIG. 16. Quadratic (B) coefficient vs the linear (A) coefficient (8) for all the second-order fits to the SRA data of Fig. 15. The straight line is a power-law least squares fitted to all of the data. The straight line with dots is power-law least squares fitted to the data for which $A < 40$. The dashed curve is a straight line least squares fitted to the data for which $A < 40$. The dotted straight line is a power-law least squares fitted to the three values (+) from the Voronovich and Zavorotny (2001) Ku-band theoretical analysis.

(R) of the backscattered power variation with incidence angle clearly increases with mss at both frequencies.

Figure 16 plots the quadratic (B) coefficient versus the linear (A) coefficient [Eq. (8)] for all second-order fits to the SRA data of Fig. 15. The straight line was least squares fitted to the log of the B and A coefficients for all data. Its equation is the power law

$$B = 0.4182A^{1.434}. \tag{22}$$

The straight line with dots was least squares fitted to the log of the B and A coefficients for all data except for the lightest wind speed day, resulting in

$$B = 0.5676A^{1.332}. \tag{23}$$

The dashed curve is actually a straight line (appearing curved due to the log–log axes in Fig. 16) that was least squares fitted to the B and A coefficients for all data except for the lightest wind speed day. Its equation is

$$B = -9.84 + 2.066A. \tag{24}$$

The dashed and solid curves indicate a very similar dependence of B on A for values of A less than 40. If the cluster of data for the 2 m s^{-1} wind speed day ($60 < A < 100$) were included in the linear dependence curve fit (24), the fit to the main body of data would have degraded significantly.

The equation of the dotted line, least squares fitted to the log of the three Ku-band values (+ symbols) from the Voronovich and Zavorotny (2001) theoretical analysis shown in Fig. 3, is

$$B = 0.4194A^{1.327}. \tag{25}$$

7. Discussion

It should be kept in mind that Figs. 13 and 16 were generated from a single dataset acquired over the course of a single week in a single wave/current/wind environment. However, the possibility that there may be a global model to characterize Ka-band radar backscatter from the sea surface within 25° of nadir is tantalizing. The onset of skewness in the backscattered power distribution between 6 and 8 m s^{-1} indicated in Fig. 13 is supported by data collected by the SRA in the very different environment of the western Pacific equatorial warm pool during the Tropical Ocean and Global Atmosphere Coupled Ocean–Atmosphere Response Experiment (TOGA COARE; Walsh et al. 1998).

Two recent Ka-band investigations of near-nadir backscatter did not comment on skewness because their ability to study it was hampered by the experiment designs. Vandemark et al. (2004) used a nonscanning nadir-directed antenna from an aircraft at 15-m height to interrogate the sea surface within a 1-m equilateral triangle of wave elevation measurements provided by three downlooking laser altimeters. The experiment was designed to study the variation of nadir backscatter with the wind and wave characteristics and its 6° (two way) antenna beamwidth could not resolve variations in skewness.

Tanelli et al. (2006) measured backscattered power at both Ka and Ku band with a scanning antenna (±25°) from a high-altitude aircraft. Their 3.4° half-power beamwidth (two way) at Ka band provided one limitation on investigating skewness. Another limitation was their forward-looking angle of 3°, which combined with an aircraft pitch attitude rarely below 1° to provide little data within 4° of nadir. All of the aircraft on which the SRA has been mounted generally flew in a 2° nose-up attitude. The SRA antenna was always mounted looking aft 2° so that the beam would scan through nadir during the flights.

Tanelli et al. indicated that they made fourth-order polynomial fits (versus θ, not $\tan^2 \theta$) to the data from only one side of the cross-track radar scan to avoid up/downwind asymmetries. But it might have been better to process both sides of the scan and try to estimate the skewness of the distribution rather than to suffer its contamination to an unknown extent. The discussion relating to Fig. 12 of this paper and Walsh et al. (1998) indicates that an undetermined skewness in the backscattered power distribution can significantly distort the interpretation of the variation of backscattered power with incidence angle and the computed mss.

Looking at the variation of backscattered power with incidence angle to the left and to the right of nadir should not produce disjoint estimates of the mss, but they will if there is undetermined skewness present. Even with the data void within 4° of nadir, if it were assumed that the backscatter were symmetrical within about 10° of the "effective" normal to the surface, the Tanelli et al. dataset might provide useful estimates of the shift in the peak of the backscattered power distribution at both Ka and Ku bands and possibly identify a frequency dependence in the shift.

The present analysis indicates that the non-Gaussian characteristic of the scattering increases as the mss increases. Figure 16 suggests that the quadratic (B) coefficient is uniquely related to the linear (A) coefficient. Except for the lightest wind day, there was considerable overlap in the A and B coefficients from day to day because they varied significantly azimuthally. But the scatter for any given day spread the coefficients along the general power law representing the entire dataset. This is important because it suggests that, for a particular value of the A coefficient, the same B coefficient will be associated with it whether the A coefficient corresponded to the crosswind direction at a high wind speed, or to the upwind direction at a lower wind speed, or to an intermediate wind speed at an intermediate direction relative to the wind.

The Voronovich and Zavorotny (2001) Ku-band theoretical analysis using Gaussian slope statistics produced almost the same power-law relationship between A and B as the SRA Ka-band observations. Further investigation is needed to determine whether the offset between the Ku-band curve fit to their theoretical results and the Ka-band data is due to a contribution of non-Gaussian slope statistics, or to the frequency difference, or to problems in the theory and/or measurements. However, what it suggests is that, whether the non-Gaussian nature of the scattering is caused by non-Gaussian slope statistics, or Gaussian slope statistics and diffraction, or some combination of the two, the linear coefficient, A, is sufficient to determine the characteristics of the backscatter.

It should be emphasized that the relationship between A and B was not obtained using off-nadir angles, but local incidence angles that took into account the slopes of waves whose wavelengths were longer than about 16 to 25 m. Computing local incidence angles is not possible for most remote sensors. But the hope is that measurements binned by off-nadir angle and averaged over areas large enough that long-wave slopes are statistically represented at all incidence angles would produce the same result. If that were shown to be the case, this simple model might prove very useful for predicting the performance of remote sensors that operate within 25° of nadir.

Acknowledgments. This analysis was supported by the NASA Physical Oceanography program and the Office of Naval Research Coupled Boundary Layers Air–Sea Transfer (CBLAST) program. Donald E. Hines of the NASA Goddard Space Flight Center maintained the SRA and provided critical support during the conduct of the experiment. David Parkin and Cecil Maher of CSIRO contributed essentially to the SRA installation on the Fokker F-27 and the conduct of the experiment. Wei Chen was instrumental in acquiring many of the atmospheric measurements and the crew of the CSIRO Fokker F-27 aircraft did an outstanding job with the complex flight patterns. E. J. Walsh thanks A. Voronovich and V. Zavorotny of the NOAA/Earth System Research Laboratory Physical Sciences Division for discussions and supplying their model output.

REFERENCES

Banner, M. L., W. Chen, E. J. Walsh, J. B. Jensen, S. Lee, and C. Fandry, 1999: The Southern Ocean Waves Experiment. Part I: Overview and mean results. *J. Phys. Oceanogr.,* **29,** 2130–2145.

Barrick, D. E., 1968: Rough surface scattering based on the specular point theory. *IEEE Trans. Antennas Propag.,* **16,** 449–454.

——, 1974: Wind dependence of quasi-specular microwave sea scatter. *IEEE Trans. Antennas Propag.,* **22,** 135–136.

Bock, E. J., and T. Hara, 1995: Optical measurements of capillary–gravity wave spectra using a scanning laser slope gauge. *J. Atmos. Oceanic Technol.,* **12,** 395–403.

Chapron, B., V. Kerbaol, D. Vandemark, and T. Elfouhaily, 2000: Importance of peakedness in sea surface slope measurements and applications. *J. Geophys. Res.,* **105,** 17 195–17 202.

Chen, W., M. L. Banner, E. J. Walsh, J. B. Jensen, and S. Lee, 2001: The Southern Ocean Waves Experiment. Part II: Sea surface response to wind speed and wind stress variations. *J. Phys. Oceanogr.,* **31,** 174–198.

Cox, C. S., and W. H. Munk, 1954: Measurement of the roughness of the sea surface from photographs of the sun's glitter. *J. Opt. Soc. Amer.,* **44,** 838–850.

Elfouhaily, T., B. Chapron, K. Katsaros, and D. Vandemark, 1997: A unified directional spectrum for long and short wind-driven waves. *J. Geophys. Res.,* **102,** 15 781–15 796.

Gotwols, B. L., and D. R. Thompson, 1994: Ocean microwave backscatter distributions. *J. Geophys. Res.,* **99,** 9741–9750.

Haimbach, S. P., and J. Wu, 1985: Field trials of an optical scanner for studying sea-surface fine structures. *IEEE J. Oceanic Eng.,* **10,** 451–453.

Huang, N. E., and S. R. Long, 1980: An experimental study of the surface elevation probability distribution and statistics of wind-generated waves. *J. Fluid Mech.,* **101,** 179–200.

Hughes, B. A., H. L. Grant, and R. W. Chappell, 1977: A fast response surface-wave slope meter and measured wind-wave moments. *Deep-Sea Res.,* **24,** 1211–1223.

Hwang, P. A., and O. H. Shemdin, 1988: The dependence of sea surface slope on atmospheric stability and swell conditions. *J. Geophys. Res.,* **93,** 13 903–13 912.

Plant, W. J., 1986: A two-scale model of short wind-generated waves and scatterometry. *J. Geophys. Res.,* **91,** 10 735–10 749.

——, 2003: A new interpretation of sea-surface slope probability density functions. *J. Geophys. Res.,* **108,** 3295, doi:10.1029/2003JC001870.

Shaw, J. A., and J. H. Churnside, 1997: Scanning-laser glint measurements of sea-surface slope statistics. *Appl. Opt.,* **36,** 4202–4213.

Tanelli, S., S. L. Durden, and E. Im, 2006: Simultaneous measurements of Ku- and Ka-band sea surface cross sections by an airborne radar. *IEEE Geosci. Remote Sens. Lett.,* **3,** 359–361.

Tang, S., and O. H. Shemdin, 1983: Measurement of high frequency waves using a wave follower. *J. Geophys. Res.,* **88,** 9832–9840.

Tatarskii, V. I., 2003: Multi-Gaussian representation of the Cox–Munk distribution for slopes of wind-driven waves. *J. Atmos. Oceanic Technol.,* **20,** 1697–1705.

Thompson, D. R., and B. L. Gotwols, 1994: Comparisons of model predictions for radar backscatter amplitude probability density functions with measurements from SAXON. *J. Geophys. Res.,* **99,** 9725–9739.

Valenzuela, G. R., 1978: Theories for the interaction of electromagnetic and oceanic waves—A review. *Bound.-Layer Meteor.,* **13,** 61–85.

Vandemark, D., B. Chapron, J. Sun, G. H. Crescenti, and H. C. Graber, 2004: Ocean wave slope observations using radar backscatter and laser altimeters. *J. Phys. Oceanogr.,* **34,** 2825–2842.

Voronovich, A. G., and V. U. Zavorotny, 2001: Theoretical model for scattering of radar signals in Ku- and C-bands from a rough sea surface with breaking waves. *Waves Random Media,* **11,** 247–269.

Walsh, E. J., L. K. Shay, H. C. Graber, A. Guillaume, D. Vandemark, D. E. Hines, R. N. Swift, and J. F. Scott, 1996: Observations of surface wave-current interaction during SWADE. *Global Atmos. Ocean Syst.,* **5,** 99–124.

——, D. C. Vandemark, C. A. Friehe, S. P. Burns, D. Khelif, R. N. Swift, and J. F. Scott, 1998: Measuring sea surface mean square slope with a 36-GHz scanning radar altimeter. *J. Geophys. Res.,* **103,** 12 613–12 628.

——, and Coauthors, 2002: Hurricane directional wave spectrum spatial variation at landfall. *J. Phys. Oceanogr.,* **32,** 1667–1684.

——, M. L. Banner, J. H. Churnside, J. A. Shaw, D. C. Vandemark, C. W. Wright, J. B. Jensen, and S. Lee, 2005: Visual demonstration of three-scale sea surface roughness under light wind conditions. *IEEE Trans. Geosci. Remote Sens.,* **43,** 1751–1762.

Wright, C. W., and Coauthors, 2001: Hurricane directional wave spectrum spatial variation in the open ocean. *J. Phys. Oceanogr.,* **31,** 2472–2488.

Wu, J., 1991: Effects of atmospheric stability on ocean ripples: A comparison between optical and microwave measurements. *J. Geophys. Res.,* **96,** 7265–7269.